Fault analysis to improve reliability of a LEO satellite EPS

E. Mostacciuolo [*] **F. Vasca,** ***Senior Member IEEE*** [*]
S. Baccari, ***Member IEEE*** [*]
L. Iannelli, ***Senior Member IEEE*** [*] **S. Sagnelli** [**] **R. Luisi** [**]
V. Stanzione [**]

[*] *Department of Engineering, University of Sannio, 82100 Benevento, Italy. Email:(eli280388@gmail.com, vasca@unisannio.it, silvio.baccari@unisannio.it, iannelli@unisannio.it.)*
[**] *SITAEL spa, 70042 Mola di Bari, Bari, Italy, (sagnelli@sitael.com, raffaele.luisi@sitael.com, stanzione@sitael.com.)*

Sommario
Small satellites are becoming popular for space missions due to the lower cost of manufacturing and deployment. The reduction of costs caused by a small over sizing of the components makes the simulation more important to estimate the behavior of the satellite both in the case of normal operation and in case of failure of some components. In this paper a safety strategy for a peak power tracker architecture with an unregulated bus is presented. The proposed policy is divided in two levels; a low level strategy determines the fault occurrences while the management of loads is demanded to the high level policy. Simulation results show the effectiveness of the proposed solution and the impact of the strategies on the fault diagnosis.

1. INTRODUCTION

The interest in small satellites is recently increased due to the lower cost compared to the efficiency of manufacture and deployment Bouwmeester and Guo (2010). Simultaneously a growing need of reliability and uninterrupted functioning of the satellite is becoming essential. As result fault detection and diagnosis and fault-tolerant control approaches in spacecraft attitude control systems have gained considerable attention within the scientific community Gao et al. (2015); Carvajal-Godinez et al. (2017).

To assure the success of a mission, it is decisive to detect any changes in the system (faults) for minimizing performance degradation and avoiding dangerous situations that may lead to a reduction in the life span or to a loss of the mission. A fault is defined as an unpermitted deviation of at least one characteristic property or parameter of the system from the acceptable or standard condition. Moreover it is possible to classify the fault according to the part of the system involved Marzat et al. (2012).

Typically the reliability is assured by mean of hardware redundancy Sukumar et al. (2016). Moreover several analytical approaches have been analyzed for the fault diagnosis relative to the attitude determination and control subsystem Hwang et al. (2010); Yin et al. (2016). Advanced diagnostic and prognostic Testbed have been developed to provide a technology-neutral basis for testing and evaluating diagnostic systems, both software and hardware Poll et al. (2007). Conversely only few papers are dedicated to carry out fault diagnosis on the electrical power system (EPS) basically due to the high complexity of the components. Indeed, the EPS should be effectively compliant to several requirements in order to provide power generation, management, storage, control, protection and distribution to the spacecraft payloads and platform equipment during the entire mission life. Nevertheless test and telemetry data of the power system are easily obtained. As result, a data driven fault diagnosis of the EPS has recently gained interest Suo et al. (2018); Barua and Khorasani (2011). In order to assure the autonomy of the satellite, typically these fault diagnosis operations, based on system monitoring through the available on-board observations, are followed by recovery procedures.

In this paper we focus on the power management policy aimed to the system reliability. The power tracker (PPT) topology with unregulated bus for the EPS of a low Earth orbit (LEO) small satellite is then considered and modelled as in the former authors work Mostacciuolo et al. (2018). An implemented high-level supervisor is responsible of the faults detection by monitoring the main bus voltage. Once the fault has been detected, the supervisor decides if the satellite needs to be switched to a "safe mode" or if it can works normally. The safe mode is achieved by shutting down non-essential loads.

The paper is organized as follows. In Section 2 the EPS architecture is recalled, by detailing the tuning process underlying the battery parameters. Section 3 deals with the EPS control subsystems and the power management policy. Section 4 presents the proposed safety policy and the simulation results are discussed in Section 5. Finally, in Section 6 the research conclusions are summarized.

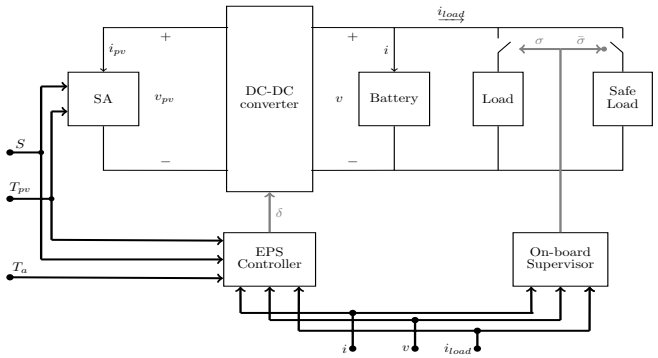

Figura 1. Fault tolerant EPS architecture.

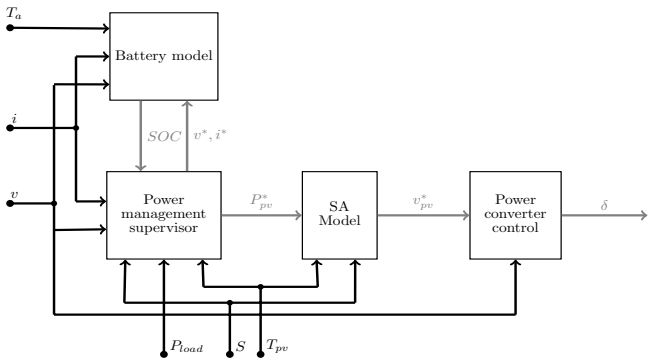

Figura 2. Block scheme of the EPS controller.

2. FAULT TOLERANT ELECTRICAL POWER SYSTEM ARCHITECTURE

The modular architecture for the implemented fault tolerant system with regard to the analyzed PPT unregulated bus architecture is shown in Fig. 1. The main blocks are: the solar array (SA), the DC-DC power converter, the battery pack, the loads, the EPS controller and the on-board supervisor. In the analyzed topology the battery pack is connected in parallel with the output voltage of the DC-DC converter so as the loads. The SA is made up of several PV panels, each one composed by a certain number of PV cells connected in a series–parallel combination. The solar irradiance S and the temperature T_{pv} are considered as exogenous inputs for the SA model. Moreover the sum of the currents obtained by the n_p parallel cells, i.e. $i_{pv} = \sum_{c=1}^{n_p} i_{pv_c}$ is regarded as a further input, while the sum of the n_s series cells voltage, i.e., $v_{pv} = \sum_{c=1}^{n_s} v_{pv_c}$ is the output of the SA model. The EPS controller determines the power converter duty cycle δ by using as inputs the battery voltage v, the battery current i, the ambient-temperature T_a, the PV temperature T_{pv}, the irradiance S and the loads power P_{load}. The on-board supervisor monitors the system through the measurements of the loads current, battery voltage and current, i.e. i_{load}, i, v, respectively. If a fault occurs and is detected, according to the information obtained the supervisor provides the necessary change by eventually enabling the safe load. The EPS controller and the on-board supervisor will be further detailed in the following sections.

3. ELECTRICAL POWER SYSTEM

The EPS controller, shown in Fig. 2, consists of a dynamic battery model, a power management supervisor, a SA model and a power converter control that allow to determine the duty cycle δ corresponding to the nominal converter input/output steady state characteristic during the sunlight. In the following subsections the main blocks are detailed.

3.1 Battery model

The battery dynamic is modeled by considering the state of charge SOC and the battery temperature T as state variables. The state of charge is determined by integrating the nonlinear differential equation

$$\frac{\mathrm{d}}{\mathrm{d}t} SOC = \frac{1}{C(T,i)} i, \tag{1}$$

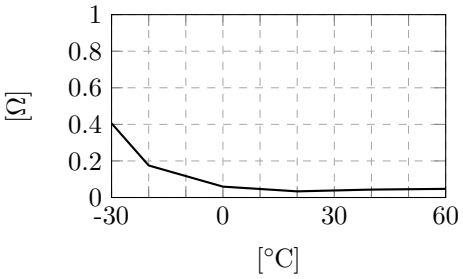

Figura 3. Resistance $R(T)$ of the battery pack.

where C is the battery capacitance which depends on the battery internal temperature T and on the current Mostacciuolo et al. (2018). The battery internal temperature is given by the following equation:

$$C_{th} \frac{\mathrm{d}}{\mathrm{d}t} T = -\frac{1}{R_{th}} (T - T_a) + R(T) i^2 \tag{2}$$

where R_{th} and C_{th} are the thermal resistance and the thermal capacitance, respectively, T_a is the ambient temperature and R is the temperature-dependent internal resistance. The term $P_{diss} = R(T)i^2$ is the power dissipated due to the Joule effect.The battery voltage v depends on i, T and SOC through the open circuit voltage E_{oc}. In particular, one can write

$$v = E_{oc}(SOC, T) + R(T) i \tag{3}$$

where E_{oc} is a nonlinear function of SOC and T Farmann and Sauer (2017). The battery current and voltage has the role of input and output of the EPS controller model and their roles swap according to the specific phase of the battery charging algorithm.

The EPS model parameters have been tuned on a realistic LEO satellite mission. The battery datasheet provides the nonlinear map $R(T)$ which is shown in Fig. 3. During the tests the temperature was obtained by integration of (2) with $R_{th} = 1.8\,\mathrm{KW}^{-1}$ and $C_{th} = 260\,\mathrm{JK}^{-1}$.

The map $C(T, i)$ is obtained with some elaborations on experimental data. The discharging characteristics of the battery voltage are assumed to be known for different constant discharging currents. An example is shown in Fig. 4 where each curve corresponds to a different (regulated) ambient temperature and all curves are for the same current $\bar{i}$. Since the discharging current is constant, on the horizontal axis one can see the time during the discharging phases, starting at 0 with full charge ($SOC = 1$) till the complete discharge, i.e. minimum battery voltage

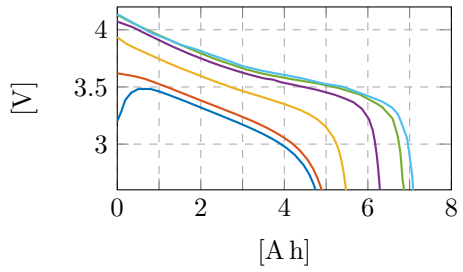

Figura 4. Discharging battery characteristics for different ambient temperatures at $C/5$ ($T_a = -35\,°C$ blue, $-30\,°C$ red, $T_a = -20\,°C$ yellow, $T_a = 0\,°C$ violet, $20\,°C$ green, $40\,°C$ cyan).

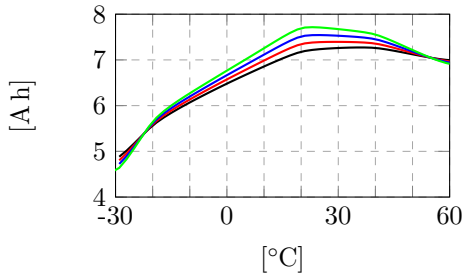

Figura 5. Characteristics $C(T, i)$ of the battery; $i = 10\,A$ black, i=20 A purple, $i = 30\,A$ blue, $i = 40.8\,A$ green.

and $SOC = 0$. Say $\bar{\Delta}$ the discharging phase duration which depends on T_a. During each experiment the battery temperature increases starting from the initial value which is assumed to be equal to the ambient temperature T_a. The final temperature of each experiment, say $\bar{T}$, is obtained from the thermal model (2) where the time duration of the discharging phase is known from the corresponding curves. Therefore the final point of each curve on the horizontal axis provides the value for $C(\bar{T}, \bar{i})$ where $\bar{i}$ is the positive current of that specific test.

From each experiment one can also obtain $C(T_a, \bar{i})$, i.e. the capacitance at the beginning of each discharging experiment. Indeed, by integrating (1) one can write

$$SOC(\bar{\Delta}) - SOC(0) = \bar{i} \int_0^{\bar{\Delta}} \frac{1}{C(T, \bar{i})} \mathrm{d}t = -1. \quad (4)$$

For each experiment we assume a piece-wise linear dependence of the battery capacitance with respect to the temperature:

$$C(T, \bar{i}) = \frac{C(\bar{T}, \bar{i}) - C(T_a, \bar{i})}{\bar{T} - T_a}(T - T_a) + C(T_a, \bar{i}) \quad (5)$$

where $C(T_a, \bar{i})$ is unknown. By combining (4) and (5) one obtains

$$C(T_a, \bar{i}) = C(\bar{T}, \bar{i}) + \bar{i}(\bar{T} - T_a) \int_0^{\bar{\Delta}} \frac{1}{T(t) - T_a} \mathrm{d}t \quad (6)$$

where the variation of T during the experiment can be obtained from the thermal equation (2). Then for each current $\bar{i}$ and for each ambient temperature T_a, one can obtain two values of the map $C(T, \bar{i})$, i.e. $C(\bar{T}, \bar{i})$ and $C(T_a, \bar{i})$. By repeating the same arguments for all tests one obtains the points of the map $C(T, i)$ which is shown in Fig. 5.

The map $E_{oc}(SOC, T)$ shown in Fig. 6 is determined

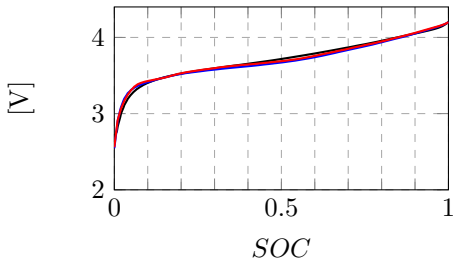

Figura 6. E_{oc}[V] vs SOC for different T ($T = -15\,°C$ black, $T = 25\,°C$ blue, $T = 55\,°C$ red).

from (3) by using producer experimental data of v, i, T and SOC of dedicated experimental tests.

3.2 SA model

Each cell of the SA can be represented by an equivalent electrical circuit where the cell acts as a current source shunted by an ideal diode Villalva et al. (2009). By assuming that all cells are equal, the PV panel voltage is the sum of the voltages provided by the series-connected cells, i.e. $v_{pv} = n_s v_{pv_c}$, while the PV panel current is the sum of the currents of the parallel-connected cells, i.e. $i_{pv} = n_p i_{pv_c}$. In particular, one can write

$$i_{pv} = f(i_{pv}, v_{pv}, T_{pv}, S) \quad (7)$$

with

$$f(i_{pv}, v_{pv}, T_{pv}, S) = n_p i_{ph}(T_{pv}, S) - I_0(T_{pv}) n_p \left[e^{\frac{\sigma}{T_{pv}} \left(\frac{v_{pv}}{n_s} + \frac{R_s i_{pv}}{n_p} \right)} - 1 \right] - \frac{n_p v_{pv} + n_s R_s i_{pv}}{n_s R_{sh}} \quad (8)$$

where i_{ph} is the photo-generated current, I_0 is the diode saturation current, $\sigma = q/(nK)$ with q the electron charge, n the diode ideality factor and K the Boltzmann constant. R_s represents the internal resistance to the current flowing, due to the resistivity of the material. The shunt resistor R_{sh} determines the leakage current across the junction. By writing the PV current in terms of its voltage and power and by substituting $i_{pv} = P_{pv}/v_{pv}$ in (7) one can write

$$P_{pv} = v_{pv} f(P_{pv}/v_{pv}, v_{pv}, T_{pv}, S). \quad (9)$$

The considered EPS consists of four equal PV panels. Each PV panel is composed by $n_s \times n_p$ cells with $n_s = 22$ and $n_p = 10$. The current-voltage characteristic of a single cell is reported in Fig. 7. The resistances $R_s = 0.04\,\Omega$ and $R_{sh} = 73\,k\Omega$, and the ideality factor $n = 3.45$ have been determined from the cell datasheet by using the iterative Newton-Raphson method Mostacciuolo et al. (2018).

4. EPS MANAGEMENT

4.1 Power management supervisor

The power management policy is synthesized by a finite state machine shown in Fig. 8.

The inputs of the algorithm are the irradiance S for each panel and the temperature T_{pv}, the measured battery voltage v and current i, the load demand P_{load}, and the battery state of charge SOC. The SOC is evaluated through the integration of the battery model described

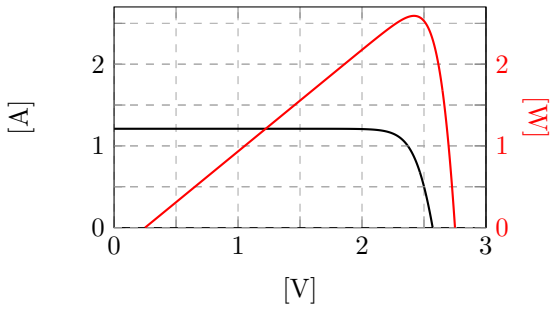

Figura 7. PV cell characteristics: i_{pv_c} vs v_{pv_c} (black line) and P_{pv_c} vs v_{pv_c} (red line).

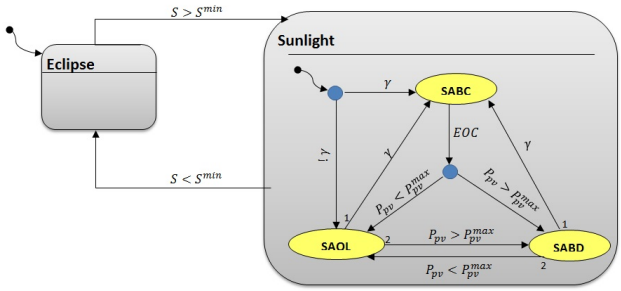

Figura 8. Finite-state machine of the power management supervisor.

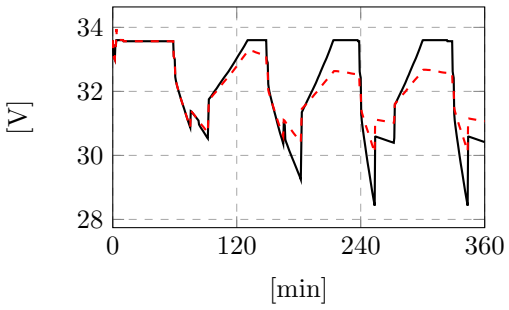

Figura 9. Measured and expected battery voltage in case of fault. In particular, v^* and v correspond to black and dashed red lines, respectively.

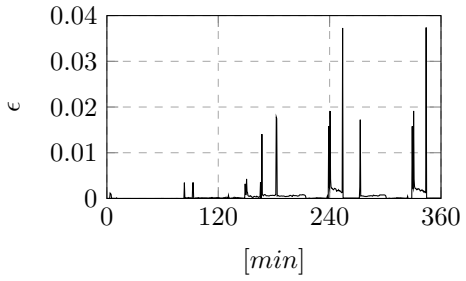

Figura 10. Derivative of the error between measured and expected battery voltage in case of fault.

in Sect. 3.1. The output of the finite-state supervisor are the desired PV power, say P_{pv}^*, that the SA should supply and the reference values v^* and i^* for the battery voltage and the battery current, respectively. During the sun eclipse phase, the battery is the only power source for the satellite. The finite-state supervisor commutes between the two states representing the eclipse and the full power phases by the mean of a selected threshold irradiance.

The complexity of this policy lies in attempting to balance two potentially conflicting objectives. Indeed, during sunlight, the SA management has to satisfy the payloads power demand and to ensure the full charge of the battery. Moreover it should be considered that the battery can be used to sustain the payloads power demand when the latter exceeds the SA capability. During the sunlight phase, the power management policy is characterized by three states according to different operating conditions of the satellite: SA only loads, SA battery discharging and SA battery charging Mostacciuolo et al. (2018).

4.2 Safety policy

The sudden load change and the cycle numbers for batteries charge and discharge are among the causes of fault and consequently of failures of the whole power electrical system. To avoid the possible failure, the on-board computer monitors the main bus voltage and current. The implemented system is split in two levels, i.e. the low and the high level, respectively. In particular the fault detection and the telemetry functionality are demanded to low level. Algorithm 1 implements the battery fault detection. The on-board supervisor compares the measured battery voltage v with the expected v^*. In Fig. 9 the evolution of v and v^* in case of fault occurrence, is depicted. When the first fault occurs the two voltage evolutions start to differ. The fault events are highlighted by a change in the derivative of the difference between the two voltages, see Fig. 10. A slowly changing fault would be detect, even the error at a given time instant would be small. The signal generated is sent to the high level.

Algorithm 1 Battery fault detection

Input v^*, v,
Data h, $\epsilon_{threshold}$
Output Fault detect
/*Error between the expected and the measured battery voltages, respectively*/
$\Delta_v \leftarrow v - v^*$
/*Evaluation of the error incremental ratio where h is the sampling step*/
$\epsilon(k+1) \leftarrow (\Delta_v(k+1) - \Delta_v(k))/h$
/*Computation of the error rate module*/
$\epsilon \leftarrow |\epsilon(k+1)|$
/*Check for a possible fault */
$(\epsilon > \epsilon_{threshold})$ $Faultdetect \leftarrow true$
$Faultdetect \leftarrow false$

The latter decides to activate the safe mode, according to the finite state machine in Fig. 11. Two different states can be distinguished; NORMAL_Mission and SAFE_MODE, respectively. During the healthy life-span of the satellite the NORMAL_Mission mode is active. When the signal $fault\_detect$ is true, the supervisor knows that a fault has been detected, but the system is still able to maintain the normal operation by using the oversized part of the generator and energy storage. During this phase the EPS controller by acting on the battery current i, guarantees the instantaneous power equilibrium condition

$$P_{pv} = \frac{1}{\eta} P_{load} + vi \tag{10}$$

where the load power profile P_{load} is assumed to be known, and $\eta \ll 1$ is a factor that takes into account the non ideal conditions (non unitary efficiency of the power converter

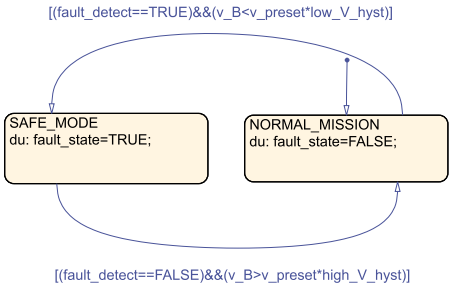

Figura 11. Finite state machine of the on-board supervisor high level.

width=6.5cm, height=4.5cm,

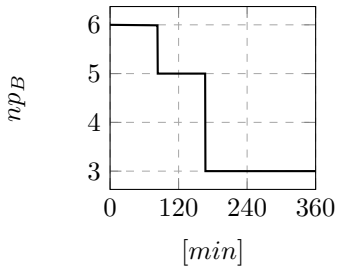

Figura 12. Injection of faults by variation of parameters np_B in battery pack.

and/or harness power losses). In order to prevent the over-discharge of the battery and the consequent lost of the mission, it monitors the main bus voltage and the battery current to decide if some load disconnection is required. Then, if the voltage $v < v\_preset\ low\_V\_hyst$ with $v\_preset = 33\,\mathrm{V}$ being the nominal main bus voltage and $low\_V\_hyst = 0.85$ a constant, the SAFE mode is activated. During this mode the high level supervisor shuts down some unnecessary loads in order to assure the power supply to critical devices. The satellite operates in safe mode until no more faults occurs and the failure is restored or the battery is enough charged, i.e. $fault\_detect == false$ and if the voltage $v > v\_preset\ high\_V\_hyst$ with $high\_V\_hyst = 0.98$.

5. SIMULATIONS

The effectiveness of the proposed safe recovery policy is demonstrated through several numerical tests. The anomaly in the battery has been simulated by the injection of an abrupt fault as shown in Fig. 12. The battery pack consists of $ns_B \times np_B$ cells. The lost of one or more string is simulated by acting on the number of parallel cells, i.e. np_B. Each fault has been injected with two levels of severity gradually increasing. A two-fault case study is presented. First SA operates at its maximum power point almost always below its maximum value. The SOC, the current and the voltage of the battery are reported in Fig. 14. In Fig. 13 the solar irradiance on the SA during trajectory, the power of the load connected to battery, the power output generated by SA, the electrical power to/from battery pack with the convention of positive power for charging phase are shown. The failures happen during the eclipse of the first and second orbit period respectively see Fig. 13. where is depicted the irradiance on the SA. In particular the first failure, consisting in the disconnection

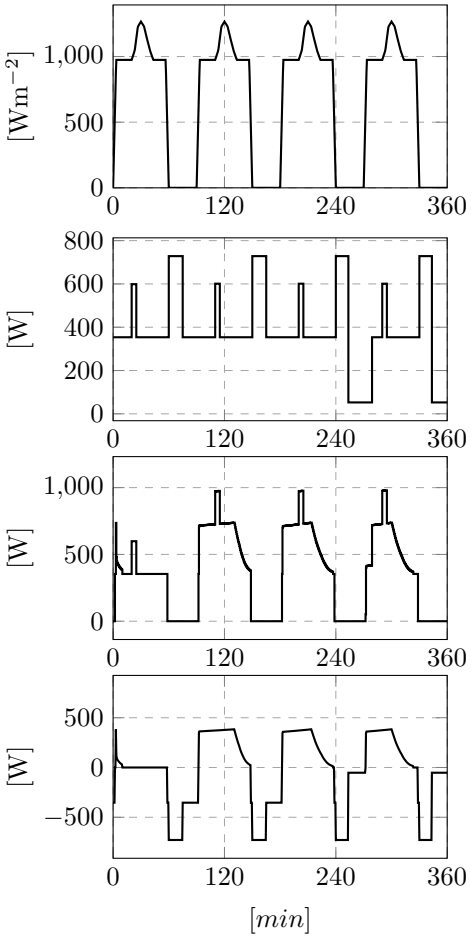

Figura 13. From top to down, the time evolution of S, P_{load}, P^*_{pv} and P_{batt}.

of one series of ns_B cells, happens at 5000 s (83 min). The second failure, consisting in the disconnection of two series of ns_B cells, occurs at 1×10^4 s (166 min). The reduction of the number of active cells in the battery pack reduces the capacity of the energy storage and increases the fluctuation of the main bus voltage see Fig. 14. Indeed a change in the slope of the v curve is evident at the time instants corresponding to the fault injection. Moreover the battery undergoes a faster discharge rate. Instead it will have high current value through the remaining active cells, in this case, a fuse guarantees that the battery cell current remains below the allowed maximum value. In the case study in Fig. 14 the battery cell current is about $2\,\mathrm{A} < I^{max}_{B_{cell}}$, with $I^{max}_{B_{cell}} = 5\,\mathrm{A}$.

Although the first failure gives rise to a consistent reduction of the energy storage capacity of the batteries, it does not result in an instantaneous activation of the safe mode Fig. 15. However during the next eclipse, the SOC decreases rapidly until it becomes critical and the battery voltage v goes under a threshold. Then the on-board computer put the satellite in the safe mode 1.52×10^4 s (253 min). During this state, the non-critical loads are disconnected from the main bus, see of Fig. 15. The normal operation mode is restored during the sunlight phase when the SA recharges the battery (resulting in an increasing of v). Indeed SOC is almost 100% and v is higher than the critical threshold, then the standard mission loads can be

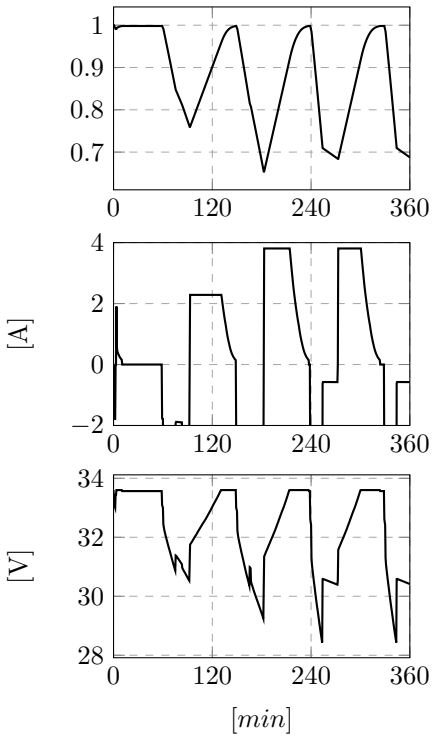

Figura 14. From top to down, the SOC, i_B^{cell} and v.

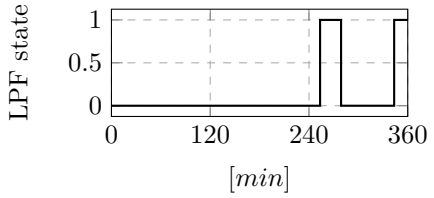

Figura 15. Actual state of the satellite; 0 and 1 indicate the normal and safe modes, respectively.

reconnected. During the next eclipse (270 min), the battery discharges until 343 min when the battery can't supply the overall power requested by the normal load. Then the supervisor enables the safe mode and the electric power consumption is reduced to the minimum $P_{load} = 50$ W.

For each panel we use typical LEO environmental conditions (e.g. temperature and irradiance). The implemented strategy to dispatch the requested power to the four panels according to the effective maximum power point has been illustrated in the former paper. The simulation duration is four orbit period, i.e. 360 minutes. The technical data and the parameters of the model are: $ns_B = 7$, $np_B = 6$, Ta =298, orbit period 5400 s (90 min), eclipse duration 1800 s (30 min), the maximum battery current is 40.8 A.

6. CONCLUSION

A fault analysis for the electrical power system of a LEO satellite has been proposed. The analysis allows one to determine a hierarchy of faults in terms of their influence on the satellite life and suitable thresholds to be assigned to the fault detector. Numerical results have shown the effectiveness of the simulator. The robustness of the simulator will be tested. Future work will consider some additional operating state, e.g. satellite start-up with a full SOC after the orbital positioning.

RIFERIMENTI BIBLIOGRAFICI

Barua, A. and Khorasani, K. (2011). Hierarchical fault diagnosis and fuzzy rule-based reasoning for satellites formation flight. *IEEE Transactions on Aerospace and Electronic Systems*, 47(4), 2435–2456.

Bouwmeester, J. and Guo, J. (2010). Survey of worldwide pico-and nanosatellite missions, distributions and subsystem technology. *Acta Astronautica*, 67(7), 854–862.

Carvajal-Godinez, J., Guo, J., and Gill, E. (2017). Agent-based algorithm for fault detection and recovery of gyroscope's drift in small satellite missions. *Acta Astronautica*, 139, 181–188.

Farmann, A. and Sauer, D.U. (2017). A study on the dependency of the open-circuit voltage on temperature and actual aging state of lithium-ion batteries. *Journal of Power Sources*, 347, 1–13.

Gao, Z., Cecati, C., and Ding, S.X. (2015). A survey of fault diagnosis and fault-tolerant techniquespart i: Fault diagnosis with model-based and signal-based approaches. *IEEE Transactions on Industrial Electronics*, 62(6), 3757–3767.

Hwang, I., Kim, S., Kim, Y., and Seah, C.E. (2010). A survey of fault detection, isolation, and reconfiguration methods. *IEEE transactions on control systems technology*, 18(3), 636–653.

Marzat, J., Piet-Lahanier, H., Damongeot, F., and Walter, E. (2012). Model-based fault diagnosis for aerospace systems: a survey. *Proceedings of the Institution of Mechanical Engineers, Part G: Journal of aerospace engineering*, 226(10), 1329–1360.

Mostacciuolo, E., Iannelli, L., Sagnelli, S., Vasca, F., Luisi, R., and Stanzione, V. (2018). Modeling and power management of a LEO small satellite electrical power system. In *16th European Control Conference*, 2738–2743. Limassol, Cyprus.

Poll, S., Patterson-Hine, A., Camisa, J., Garcia, D., Hall, D., Lee, C., Mengshoel, O.J., Neukom, C., Nishikawa, D., Ossenfort, J., et al. (2007). Advanced diagnostics and prognostics testbed. In *18th International Workshop on Principles of Diagnosis*, 178–185.

Sukumar, K., Kinger, K., John, T., Dev, A., and Shashank, K. (2016). Adaptive fault tolerant architecture for enhanced reliability of small satellites. In *IEEE Aerospace Conference*, 1–7.

Suo, M., Zhu, B., Zhou, D., An, R., and Li, S. (2018). Neighborhood grid clustering and its application in fault diagnosis of satellite power system. *Proceedings of the Institution of Mechanical Engineers, Part G: Journal of Aerospace Engineering*.

Villalva, M.G., Gazoli, J.R., and Ruppert Filho, E. (2009). Comprehensive approach to modeling and simulation of photovoltaic arrays. *IEEE Transactions on power electronics*, 24(5), 1198–1208.

Yin, S., Xiao, B., Ding, S.X., and Zhou, D. (2016). A review on recent development of spacecraft attitude fault tolerant control system. *IEEE Transactions on Industrial Electronics*, 63(5), 3311–3320.